PAPER • OPEN ACCESS

Water activation products generation and transport in DEMO divertor

To cite this article: P. Chiovaro *et al* 2024 *Nucl. Fusion* **64** 046016

View the article online for updates and enhancements.

Water activation products generation and transport in DEMO divertor

P. Chiovaro[1,*] ⓘ**, A. Quartararo**[1] ⓘ**, P. Avona**[1]**, G. Bongiovì**[1]**, P.A. Di Maio**[1]**, S. Giambrone**[1] ⓘ**, I. Moscato**[2] **and E. Vallone**[1] ⓘ

[1] Department of Engineering, University of Palermo, Viale delle Scienze, Ed. 6, 90128 Palermo, Italy
[2] Fusion Technology Department—Programme Management Unit, EUROfusion Consortium, Boltzmannstraße 2, 85748 Garching, Germany

E-mail: pierluigi.chiovaro@unipa.it

CrossMark

Abstract

In water-cooled nuclear reactors, the issue of neutron-activated products transport along the primary heat transfer system (PHTS) is very demanding, as it is a coupled neutronic/fluid-dynamic problem requiring a challenging balance between accuracy and reasonable computational time. This work addresses the transport of water activation products in large hydraulic circuits. Regarding the nuclear calculations, the assessment of the production rates of the radioisotope concentrations has been performed by Monte Carlo analyses adopting the MCNP5.1.6 code, while for the transportation calculations, an innovative method has been expressly developed. It foresees a one-dimensional nodalization, in a MATLAB-Simulink environment, of the hydraulic circuit considered with a computational fluid-dynamic (CFD) characterization (by ANSYS CFX code) of the nodes under neutron flux, that is the components where radioisotopes are formed, and the highest gradients of concentration are present. The method was compared with one-dimensional models not supported by fluid-dynamic analysis. The results of this comparison showed that in cases involving fairly complicated geometries and radioisotopes with a small half-life, CFD analyses are necessary to achieve adequate accuracy. The procedure was applied to very large and rather complex hydraulic circuits like the divertor PHTSs of DEMO fusion reactor to obtain the concentrations of the activation products of the water constituents (^{16}N, ^{17}N, ^{19}O, ^{14}C, ^{41}Ar) along such systems.

Keywords: neutronics, fluid-dynamics, DEMO divertor

(Some figures may appear in colour only in the online journal)

1. Introduction

Since the beginning of the nuclear industry, it has been known that activated corrosion products (ACPs) and water activation products are a key safety and environmental issue related to the reactor primary heat transfer system (PHTS) as they are transported beyond the bio-shields creating a gamma radiation field that is hazardous to the inspection, maintenance, and operating staff [1]. In addition, activation products in the coolant circuits must be taken into account in accidental scenarios involving some break in the loop.

This work addresses the assessment of the spatial distribution of the water activation products along large hydraulic circuits of water-cooled nuclear reactors. The water activation product concentrations are considered passive scalars and their transport in the coolant loop is a coupled neutronic/fluid-dynamic problem since the source terms of the leading

---

* Author to whom any correspondence should be addressed.

equations have a nuclear nature [2]. Such a problem is very computationally demanding, as it requires the proper balance between accuracy and reasonable computation time and in recent years it has also attracted increasing interest in the field of nuclear fusion [2–5].

Within this framework, the peculiar nuclear phenomenology involved in the studied problem allowed a first simplification with respect to the methods generally adopted for ACPs in similar situations [6, 7]. Indeed, the activation products of water are only created because of a few nuclear reactions and not by decay, which makes it possible not to resort to nuclear inventory codes and to calculate their production rate solely by means of a neutron transport calculation code. Therefore, the assessment of the production rates of the radioisotope concentrations has been performed by Monte Carlo analyses adopting the MCNP5.1.6 code [8] along with the JEFF 3.3 cross section library [9], such results are shown in section 4.

As far as the transportation calculations are concerned, an innovative method was expressly developed to address the computational difficulties associated with complex hydraulic circuits, it foresees a one-dimensional nodalization, in a MATLAB-Simulink environment [10], of the hydraulic circuit considered and a computational fluid-dynamic (CFD) three-dimensional characterization, adopting ANSYS CFX code [11], of the nodes under neutron flux, that is the components where radioisotopes are formed, and the highest gradients of concentration are present. Moreover, the in-flux components of the PHTSs are characterized by complex geometry shapes in which 3D fluid dynamic effects could lead to peculiar transport phenomena. On the other side, the ex-vessel parts of the PHTSs are made of simpler components (piping) and few complex ones as the Heat eXchangers (HXs). All the details of this method will be clarified both theoretically in section 2 and operationally in section 5.

So, five activation products of the water constituents have been considered (^{16}N, ^{17}N, ^{19}O, ^{14}C, ^{41}Ar) some details of which are summarized in table 1 [12]. In a nuclear system cooled by water, the endothermic charged-particle reactions ^{16}O (n,p) ^{16}N (with threshold energy of ∼10.2 MeV) and ^{17}O (n,p) ^{17}N (with threshold energy of ∼8.4 MeV) are the principal sources of water radioactivity during operation [13, 14]. Finally, it is observed that the issue of the reaction ^{2}H (n,γ) ^{3}H in the divertor PHTSs water has not been considered in this work. The problem of Tritium production and transport in tokamaks is very challenging as it embeds several phenomena: its production by Deuterium and/or ^{7}Li (in the divertor, related to the presence of Lithium hydroxide for water chemistry control), implantation in the plasma-facing components, permeation and so on. So, the issue related to ^{2}H (n,γ) ^{3}H reaction in water is to be considered in a larger framework beyond the scope of this paper.

^{16}N decays by emission of β particle and emits γ rays with a half-life ($T_{1/2}$) of 7.13 s while ^{17}N decays by β particles and emits neutrons with a half-life of 4.173 s. ^{17}N is also produced by the reaction ^{18}O (n,d) ^{17}N (with threshold energy of ∼14.6 MeV) even if to a very lower extent as it will be shown in the following. The activation product ^{19}O is produced by the reaction ^{18}O (n,γ) ^{19}O which already takes place at thermal

energies. Such isotope decays by β emission with subsequent γ emission 100% of the time. The γ energies are 0.20 MeV, 63% of the time and 1.36 MeV, 33% of the time. Gammas of 0.11 and 1.44 MeV are produced 6% of the time (3% and 3%, respectively). The half-life of ^{19}O is 26.47 s. ^{14}C has been also considered for its potential radiological risk as it is a pure β emitter and its half-life is very great, 5730 years. It is produced both via the reaction ^{17}O (n,α) ^{14}C and ^{14}N (n,p) ^{14}C although the concentration of ^{14}N in the coolant is rather low ($4.28 \cdot 10^{19}$ atoms per -1 kg of water can be estimated [15]) so that this second production channel is rather negligible. Similarly, ^{41}Ar was taken into consideration since, although it has a short half-life (1.83 h), it emits a high-energy γ (1.29 MeV) after decaying β. Again, the concentration of the parent isotope in the coolant is quite low, amounting to $8.06 \cdot 10^{16}$ atoms per -1 kg of water [16].

The procedure developed was applied to very large and rather complex hydraulic circuits like the divertor PHTSs of DEMO fusion reactor [17, 18] as within the research activity devoted to this system, considerable attention is paid to the coolant-related sources of radioactivity that originate when water passes through the in-flux regions of the tokamak. In this connection, section 3 reports the main information on the divertor design considered. Finally, it is pointed out that section 6 is dedicated to some rough safety observations and in the last section conclusions on the outcomes of the study are drawn.

2. Description of the method

In order to assess the spatial distribution of the water activation products concentrations, a fluid-dynamic problem must be solved by taking into account both the conservation equations for the flow and the transport equations for the radioisotopes (to be considered passive scalars), with the opportune boundary conditions. Moreover, this problem is coupled with a nuclear one as the source term of the concentration transport equations is the volumetric density of the production rate of the given isotope that has a neutronic nature since it depends on the neutron flux which can be assessed by solving the related transport equation [2].

The method adopted foresees the assessment of the spatial distribution of the water activation isotope production rates within the water domain by means of complete heterogeneous neutronic models implemented in MCNP5.1.6. As already mentioned, the fact that the constituents of water are produced by a few nuclear reactions and not by decay makes it possible not to use inventory codes and to calculate production rates just by adopting a neutron transport code.

Regarding the transport analyses, a fully 3D CFD approach to evaluate the concentration spatial distributions within very large and complex circuits is not computationally achievable and probably not suitable, so the method developed foresees a lumped parameters 1D approach based on a nodalization implemented in the MATLAB-Simulink suite. So, the following Cauchy problem is solved for the nodes which are not under neutron flux

Table 1. Water activation products considered.

Parent isotope	Reaction	Activated product	Threshold energy	$T_{1/2}$
^{16}O	(n,p)	^{16}N	10.2 MeV	7.13 s
^{17}O	(n,p)	^{17}N	8.4 MeV	4.173 s
^{18}O	(n,d)		14.6 MeV	
^{17}O	(n,α)	^{14}C	—	5730 y
^{14}N	(n,p)		—	
^{18}O	(n,γ)	^{19}O	—	26.47 s
^{40}Ar	(n,γ)	^{41}Ar	—	1.83 h

$$\begin{cases} \frac{\partial C_i(x,t)}{\partial t} + u_i \frac{\partial C_i(x,t)}{\partial x} = -\lambda C_i(x,t) \\ C_i(0,t) = C_{i-1}(x_{\text{out}},t) \qquad i = 1,2,\ldots,N \\ C_i(x,0) = 0 \end{cases} \quad (1)$$

where N is the number of the nodes, C_i is the concentration of the given radioisotope, u_i is the average speed of the water (defined as the ratio between the volumetric flow rate and the cross-sectional area of the flow), λ is the decay constant and subscripts in and out indicate the entrance and exit concentrations of each node. The solution of such a problem can be put in the following functional form which is the most suitable to address the numerical method set-up

$$C_i(x,t) = C_{i-1}(x_{\text{out}}, t - x/u_i) e^{-\lambda x/u_i}. \quad (2)$$

The underlying idea of the method is to increase the accuracy of the analysis by devoting special study to the nodes/components under neutron flux since it is in these that the production of radioisotopes takes place and where their concentration gradients are greater. These components are subjected to 3D CFD analysis by means of the ANSYS CFX code to obtain their characterisation in terms of concentration. Basically, the results of these analyses are used to set up functions of the type:

$$C_i(x_{\text{out}}, t) = f[C_i(0, t - \tau_i)] \quad (3)$$

(τ_i is the transit time of water in the ith node) for each component under consideration, which are then implemented in MATLAB-Simulink to characterise the nodes under neutron flux and thus complete the modelling of the hydraulic circuit.

So, more generally, each node is characterised with the following functional form:

$$C_i(x_{\text{out}}, t) = \left[C_i(0, t - \tau_i) + \int_{t-\tau_i}^{t} R_i(t') e^{-\lambda t'} dt' \right] e^{-\lambda \tau_i},$$
$$i = 1, 2, \ldots, M \quad (4)$$

where R_i is the volumetric density of the radioisotope production rate in the ith node where it is uniform, and M is the total number of nodes in which the circuit has been modelled. Naturally, R_i is zero for the N nodes not under flux and it is different from zero in the others.

The type of the functional form of R_i can be considered the same as the DEMO source [19] whose duty cycle is characterized by a sequence of pulses, each comprising a 100 s ramp-up

transient, a 7200 s—long flat-top phase, a ramp-down transient of 100 s, and a 600 s dwell phase [20]. So, if R_i is approximated to a square wave and since the pulse duration is much higher than the circuit transit times, equation (4) can take the following form during the flat-top phase

$$C_i(x_{\text{out}}, t) = C_i(0, t - \tau_i) e^{-\lambda \tau_i} + \frac{R_i}{\lambda} \left(1 - e^{-\lambda \tau_i}\right). \quad (5)$$

The concept of transit time introduced above deserves specific consideration, as it is of uttermost importance to the accuracy of the numerical method just described. There are different approaches to define this quantity, such as simple by-hand calculations of the ideal transit time [21], that can be estimated as

$$\tau_{\text{ideal}} = V/\dot{Q}. \quad (6)$$

where V is the coolant volume and $\dot{Q}$ the volumetric flow rate, and several computational techniques best suited for complex geometries [4, 22]. The transit time inside the PHTS components characterized by simple geometries can be evaluated with by-hand calculations, i.e. as the ratio of the length of the path travelled by the water in the specific component to its average speed, while for the divertor in-vessel cooling circuits a more rigorous approach is required. Additionally, effective values for the R_i are considered for in-flux components as result of the CFD characterization discussed in section 5.

3. DEMO divertor outline

In a power plant scale fusion reactor like DEMO, a highly efficient cooling system is required for the divertor due to the large amount of thermal power it must withstand, this is why considerable research and development effort is concentrated on all aspects of this component.

As a reference, the baseline 2019 design [23] of the DEMO divertor has been taken into account. It consists of 48 toroidal assemblies (divertor cassettes), each one includes a Cassette Body (CB), endowed with a Liner and two Reflector Plates (RPs), that supports two Plasma-Facing Components (PFCs). These latter are named Inner and Outer Vertical Target (IVT, OVT), and are comprised of actively cooled Plasma Facing Units (PFUs). The cooling scheme consists of two circuits designed to independently cool the Eurofer components (CB, Liner and RPs) and the PFCs (figure 1).
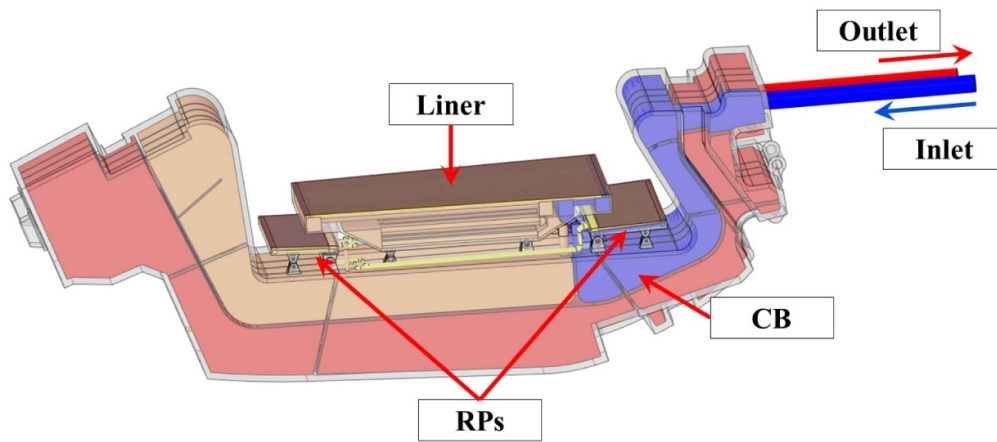
(a)
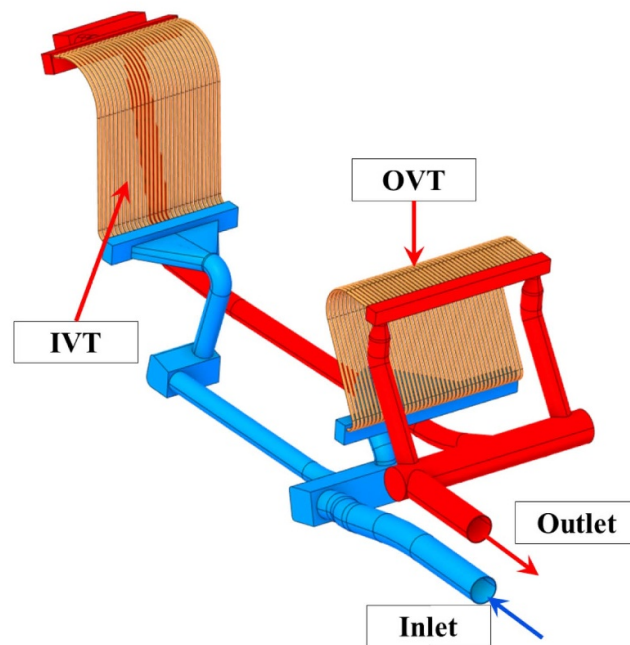
(b)

Figure 1. Divertor main components and cooling circuit adopted for the CB (*a*) and the PFCs (*b*).

Further details of the divertor architecture can be found in [24, 25].

So, the current divertor design conceives two separate functional zones, namely the PFCs and the CB, for the in-vessel component. Due to the different requirements, water coolant adopted for the two zones is at different thermal-hydraulic conditions, thus two separate PHTSs have been foreseen in the overall project, each system made of one loop providing bi-directional flow. Figure 2 shows a sketch of one of the divertor PHTSs including two HXs and a PRessuriZer (PRZ).

Then, the divertor is fed through the tokamak lower ports, therefore main water distribution will be carried out into the lower pipe chase where ring headers are placed. However, the main equipment of the coolant systems will be located in the upper levels of the tokamak building. Hot and cold legs, connecting the main equipment to the headers, will be routed through a vertical shaft. Finally, it should be noted that the main data required to carry on this study, concerning the geometry of the hydraulic circuits, mass flow rates and the thermophysical properties of the cooling water, were taken from [26, 27].
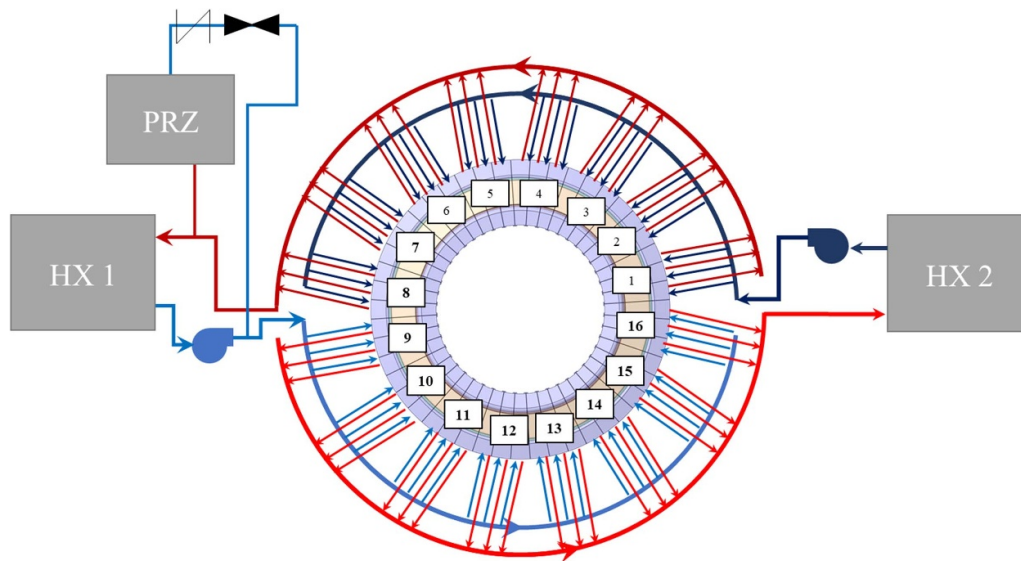
Figure 2. Conceptual arrangement for both divertor PFCs and CB PHTSs.

4. Neutronic results

A DEMO MCNP model with a fully heterogeneous double-circuit divertor (PFCs and CB) developed at ENEA-Frascati Labs (extensively described in [28]) was used together with a peculiar neutron source simulating the D-T plasma.

Regarding the material compositions, EUROfusion recommendations have been pursued [29], while concerning water, the complete isotopic composition of hydrogen and oxygen has been selected while the presence of ^{14}N and ^{40}Ar was neglected as the typical concentrations are so low that they do not alter the neutron spectrum. Figure 3 shows a detail of a poloidal-radial section of the divertor model.

The volume densities of the production rates of the isotopes considered, as mentioned above, are the starting point for the fluid-dynamic analyses with which concentration maps along both in-vessel and ex-vessel hydraulic circuits were determined. To this end, neutron analyses were conducted by dividing the entire divertor water domain with an albeit rough grid with −4 radial and −10 poloidal regions, while no toroidal divisions were considered. DEMO reactor results have been normalized using a neutron yield of $7.095 \cdot 10^{20}$ n s^{-1} which is related to the plasma flat-top phase of the pulsed operation of DEMO [20] and corresponds to a fusion power of 1998 MW [30].

Results obtained were elaborated by ANSYS CFX, figures 4–7 show results obtained in the PFC cooling circuit, figures 8–11 those in the CB cooling circuit.

As can be easily observed, the production rate of ^{17}N from ^{18}O is −4 orders of magnitude lower than the production channel via ^{17}O and, therefore, completely negligible. Similarly, the production rate of ^{14}C from ^{14}N is −2 orders of magnitude lower than the production channel via ^{17}O.

It is also interesting to observe that the various production rates have their maximum values in different areas for the same component. The production rates associated with endothermic
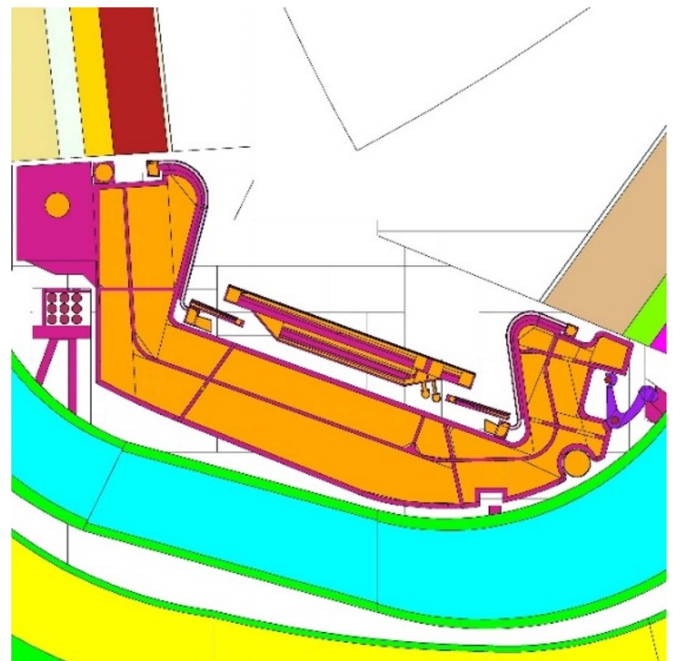

Figure 3. Poloidal—radial section of the MCNP divertor model.

reactions have their maximum values in plasma-facing zones while the rates associated with exothermic reactions in more shielded zones where the neutron spectrum is softer. An exception is the ^{19}O production rate because the reaction (n,γ) for ^{18}O has pronounced, broad resonance peaks at energies of the order of 1 MeV.

For the sake of completeness, some integral results are reported: the total neutron flux in table 2 together with the water activation product reaction rates in the main components of the divertor in table 3. It is noted that such integral data can provide data for rough but fast future assessments to help the design development.

Figure 4. ^{16}N (left) and ^{19}O (right) production rates in the PFCs.

Figure 5. ^{17}N production rates from ^{17}O (left) and ^{18}O (right) in the PFCs.

Figure 6. ^{14}C production rates from ^{17}O (left) and ^{14}N (right) in the PFCs.

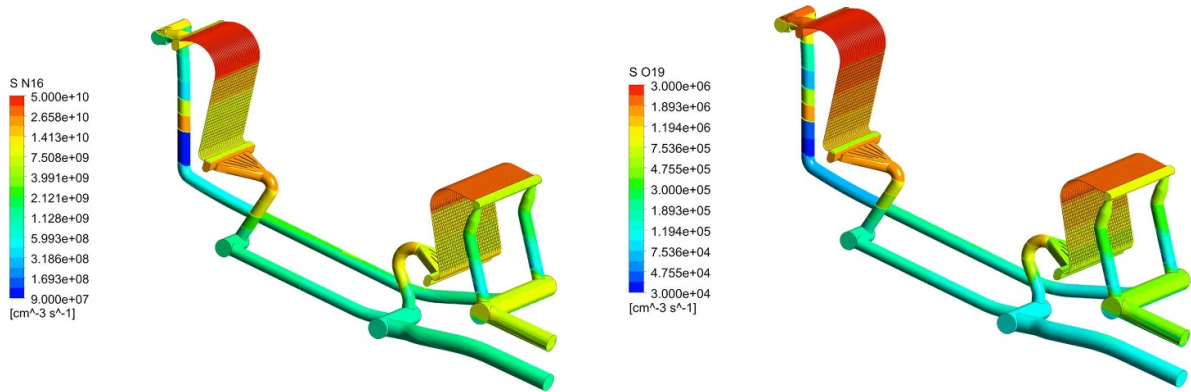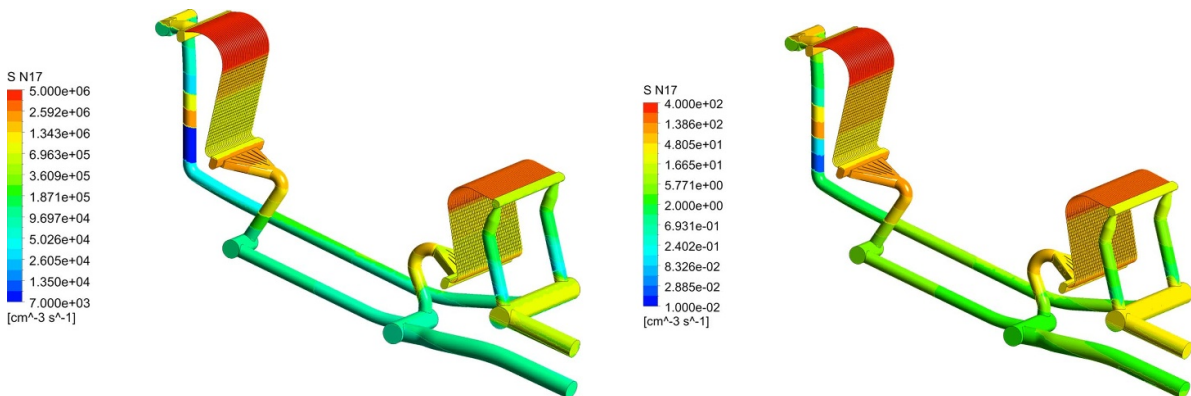**Figure 7.** ^{41}Ar production rate in the PFCs.

Figure 8. ^{16}N (left) and ^{19}O (right) production rates in the CB.

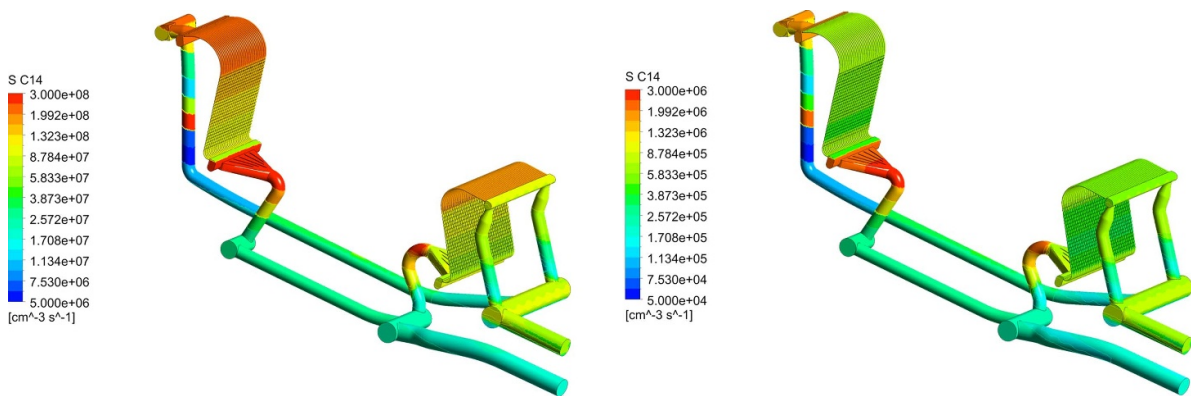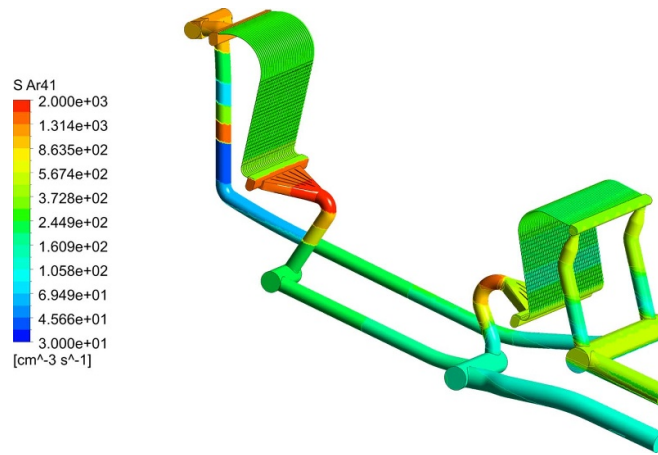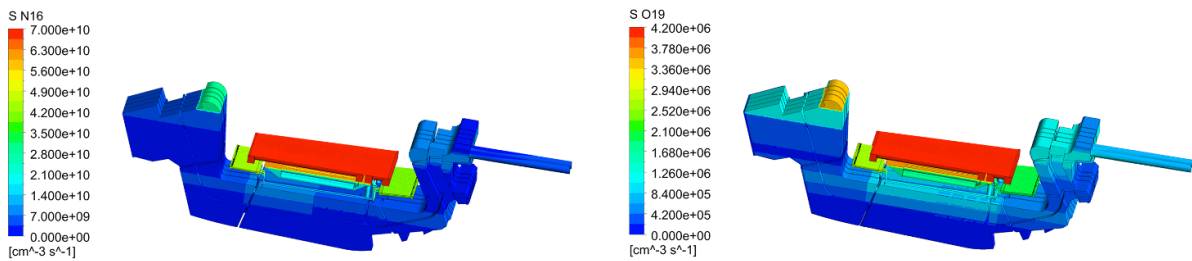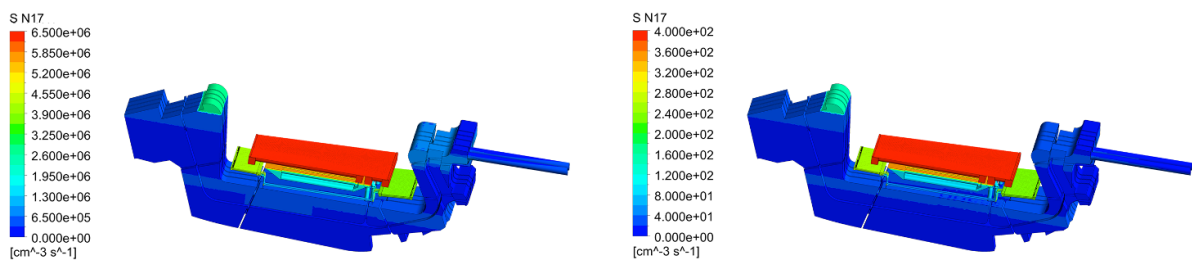**Figure 9.** ^{17}N production rates from ^{17}O (left) and ^{18}O (right) in the CB.
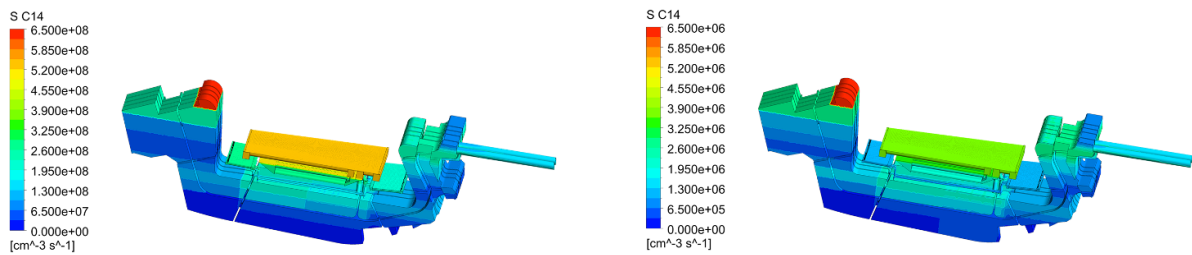

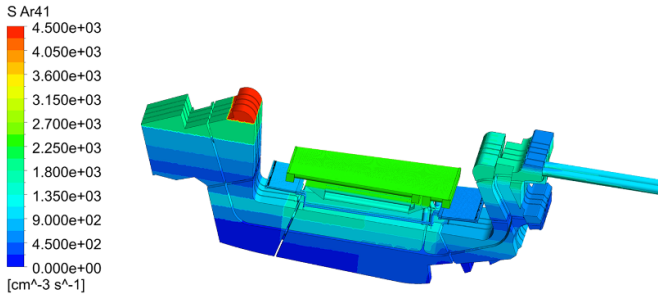**Figure 10.** ^{14}C production rates from ^{17}O (left) and ^{14}N (right) in the CB.

Figure 11. ^{41}Ar production rate in the CB.

Table 2. Total neutron flux $(\mathrm{cm}^{-2}\,\mathrm{s}^{-1})$.

OVT	$2.400 \cdot 10^{14}$
IVT	$3.016 \cdot 10^{14}$
PFC pipes	$4.702 \cdot 10^{13}$
CB	$4.296 \cdot 10^{13}$
Inner RP	$2.304 \cdot 10^{14}$
Outer RP	$1.871 \cdot 10^{14}$
Liner	$3.004 \cdot 10^{14}$

Table 3. Water activation product reaction rates per cassette (s^{-1}).

	^{16}N	^{17}N	^{14}C	^{19}O	^{41}Ar
OVT	$1.096 \cdot 10^{14}$	$1.042 \cdot 10^{10}$	$6.341 \cdot 10^{11}$	$7.993 \cdot 10^{9}$	$1.294 \cdot 10^{6}$
IVT	$8.823 \cdot 10^{13}$	$8.392 \cdot 10^{9}$	$6.083 \cdot 10^{11}$	$8.074 \cdot 10^{9}$	$1.190 \cdot 10^{6}$
PFC pipes	$7.692 \cdot 10^{14}$	$7.118 \cdot 10^{10}$	$1.083 \cdot 10^{13}$	$6.765 \cdot 10^{10}$	$6.311 \cdot 10^{7}$
CB	$4.389 \cdot 10^{15}$	$3.961 \cdot 10^{11}$	$1.451 \cdot 10^{14}$	$6.701 \cdot 10^{11}$	$1.077 \cdot 10^{9}$
Inner RP	$2.121 \cdot 10^{14}$	$2.009 \cdot 10^{10}$	$1.358 \cdot 10^{12}$	$1.266 \cdot 10^{10}$	$3.886 \cdot 10^{6}$
Outer RP	$2.743 \cdot 10^{14}$	$2.596 \cdot 10^{10}$	$1.568 \cdot 10^{12}$	$1.421 \cdot 10^{10}$	$4.327 \cdot 10^{6}$
Liner	$5.829 \cdot 10^{15}$	$5.485 \cdot 10^{11}$	$5.342 \cdot 10^{13}$	$3.870 \cdot 10^{11}$	$2.553 \cdot 10^{8}$

In this regard, it is noted that the ratio of homologous data in tables 2 and 3 provides effective macroscopic cross section values that could be useful for rough neutron calculations during design.

5. Transport analysis results

As mentioned above, fluid-dynamic transport analyses of water activation products were carried out in two separate steps and involved both the PFCs and CB cooling circuits. The first step involved the fluid-dynamic characterization of the two divertor cooling circuits by means of fully three-dimensional CFD analyses performed by ANSYS-CFX. The second step involved evaluating the concentration distribution of the studied radioisotopes in the PFCs and CB cooling circuits by means of lumped-parameter one-dimensional calculations implemented on MATLAB-Simulink.

Table 4. Inlet concentration range (m^{-3}).

Nuclide	PFCs concentration range	CB concentration range
^{16}N	0–$5.0 \cdot 10^{15}$	0–$1.0 \cdot 10^{17}$
^{17}N	0–$5.0 \cdot 10^{14}$	0–$1.0 \cdot 10^{12}$
^{19}O	0–$5.0 \cdot 10^{14}$	0–$1.0 \cdot 10^{15}$
^{41}Ar	0–$5.0 \cdot 10^{15}$	0–$1.0 \cdot 10^{14}$

5.1. CFD characterization

The fluid-dynamic studies of the PFCs and CB cooling circuit were assessed by running steady-state CFD analyses, according to the coolant operative conditions and using the neutronic results discussed above. The details of the mesh setup and the assumptions of the models are fully reported in [24, 25], with the only exception of cooling circuit mass flow rates that have been updated due to a re-assessment of the thermal loads expected for the cassette [31], and in agreement with the current divertor PHTSs specifications [26, 27]. In particular, the mass flow rate fed to each single cassette has been considered equal to 28.8 and 114.9 kg s^{-1}, respectively for the CB and for the PFCs. In this regard, it should be clarified that the analyses were carried out in an isothermal regime, taking the average between inlet and outlet temperatures of the two components considered, PFCs and CB, as reference temperatures. In the case of the PFCs cooling circuit, this choice is justified by the small temperature difference between inlet and outlet (7 °C), which induces negligible density changes. In the case of CB, this temperature difference is much higher, 30 °C, and the use of the average temperature defined above is the result of a compromise between calculation accuracy and computational burden.

3D spatial distributions of the radioisotopes considered were assessed both in the PFCs and CB cooling circuits and the related characterization functional form (equation (3)) were obtained with the best fitting of at least five inlet concentrations for each nuclide for each component. Table 4 shows the range of inlet concentration for each nuclide, the maximum values of which were evaluated by 1D preliminary transport analyses.

Figures 12–15 show the spatial distributions of such nuclides with a null inlet concentration respectively for the PFCs and the CB cooling circuits.

It is interesting to observe how, in the case of the PFCs cooling circuit, the concentration of the considered nuclides always increases from the inlet to the outlet of the cooling circuit, with the only exception of the outlet manifold, where the coolant is collected from IVT and OVT and therefore there is a mixing of the two fluid veins, which causes an average concentration value to be reached at the PFC cooling circuit outlet.

On the other hand, from figures 14 and 15 it can be argued that for long-lived nuclides there is an increase of the concentration from the inlet to the outlet of the cooling circuit, excepting for some recirculation regions where local accumulation of the isotopes is observed, while for short-lived species, the maximum concentration is reached in the lower part of the

Figure 12. ^{16}N (left) and ^{17}N (right) concentration in the PFCs cooling circuit considering a null inlet concentration.

Figure 13. ^{19}O (left) and ^{41}Ar (right) concentration in the PFCs cooling circuit considering a null inlet concentration.

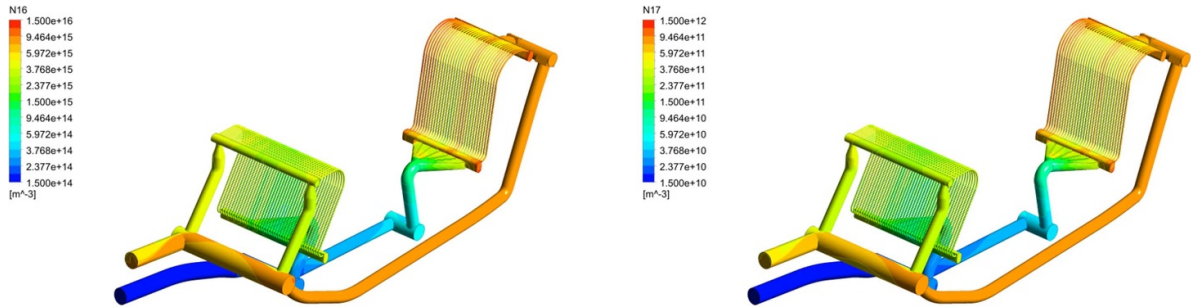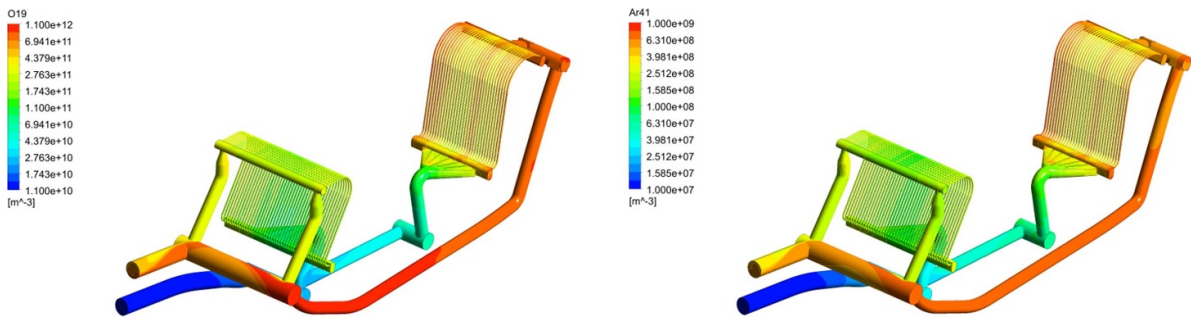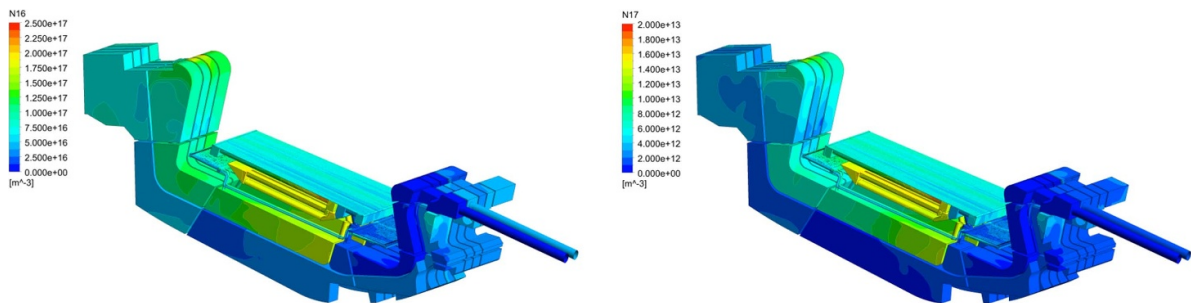**Figure 14.** ^{16}N (left) and ^{17}N (right) concentration in the CB cooling circuit considering a null inlet concentration.
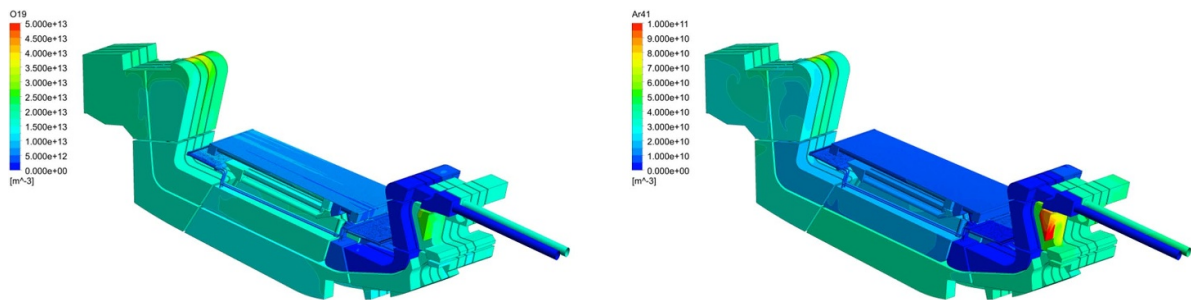
Figure 15. ^{19}O (left) and ^{41}Ar (right) concentration in the CB cooling circuit considering a null inlet concentration.

Table 5. Interpolation parameters of the PFCs CFD results.

	m	q (m^{-3})	τ_{eff} (s)	τ_{ideal} (s)	R_{eff} $(m^{-3}\,s^{-1})$	R_{ideal} $(m^{-3}\,s^{-1})$
^{16}N	$8.83 \cdot 10^{-1}$	$7.26 \cdot 10^{15}$	1.27	1.30	$6.06 \cdot 10^{15}$	$6.06 \cdot 10^{15}$
^{17}N	$8.10 \cdot 10^{-1}$	$6.42 \cdot 10^{11}$	1.27	1.30	$5.61 \cdot 10^{11}$	$5.64 \cdot 10^{11}$
^{19}O	$9.66 \cdot 10^{-1}$	$6.43 \cdot 10^{11}$	1.34	1.30	$4.89 \cdot 10^{11}$	$5.07 \cdot 10^{11}$
^{41}Ar	$9.99 \cdot 10^{-1}$	$1.42 \cdot 10^{9}$	10.91	1.30	$1.30 \cdot 10^{8}$	$4.03 \cdot 10^{8}$

Table 6. Interpolation parameters of the CB CFD results.

	m	q (m^{-3})	τ_{eff} (s)	τ_{ideal} (s)	R_{eff} $(m^{-3}\,s^{-1})$	R_{ideal} $(m^{-3}\,s^{-1})$
^{16}N	$2.53 \cdot 10^{-2}$	$3.91 \cdot 10^{16}$	37.82	44.33	$3.90 \cdot 10^{15}$	$7.39 \cdot 10^{15}$
^{17}N	$2.96 \cdot 10^{-3}$	$1.94 \cdot 10^{12}$	35.02	44.33	$3.23 \cdot 10^{11}$	$6.84 \cdot 10^{11}$
^{19}O	$3.38 \cdot 10^{-1}$	$1.64 \cdot 10^{13}$	42.37	44.33	$6.34 \cdot 10^{11}$	$7.41 \cdot 10^{11}$
^{41}Ar	$9.94 \cdot 10^{-1}$	$4.02 \cdot 10^{10}$	53.54	44.33	$7.53 \cdot 10^{8}$	$9.12 \cdot 10^{8}$

Liner and the combined effect of decay and low volumetric sources lead to a lower concentration at the outlet of the cooling circuit.

As far as the interpolation curves are concerned, they are all linear functions:

$$C_i (x_{out}, t) = m \cdot C_i (x_{in}, t - \tau_i) + q \tag{7}$$

whose parameters, slope (m) and intercept (q), acquire a special significance with regard to equation (5). Therefore, the following relations hold

$$m = e^{-\lambda \tau_{eff}} \tag{8}$$

$$q = \frac{R_{eff}}{\lambda} \left(1 - e^{-\lambda \tau_{eff}}\right). \tag{9}$$

These relations allow the calculation of effective values for transit times (τ_{eff}) and production rates (R_{eff}) of PFCs and CB, to be implemented in the MATLAB-Simulink 1D model so that to include in-flux nodes of the nodalisation of PHTSs. Tables 5 and 6 show interpolation parameters and both effective and ideal values of interest, respectively for PFCs and CB.

As can be argued from the tables, the effective transit time for the PFCs cooling circuit is close to the τ_{ideal} value of 1.30 s for the first three species, and similar considerations can be done also by comparing R_{eff} with R_{ideal}, defined as the volume-averaged product rates that can be drawn starting from the integral data reported in table 3. Concerning the ^{41}Ar, the obtained high transit time value is most likely related to the m value close to 1, leading to a τ_{eff} calculated from equation (8) very sensible to round-offs and tolerances in the calculated outlet concentration values. However, the influence of this parameter on the results is negligible, as the product $\lambda \tau_{eff}$ is in any case close to zero for the ^{41}Ar.

Regarding the CB cooling circuit, similar reasoning is applicable for the ^{41}Ar, while more interesting results are instead obtained for the other species. In particular, the lower is the nuclide half-life, the shorter is the calculated effective

transit time, while the ideal transit time for the cassette is 44.33 s.

As a general trend, it can be observed that with low values of the product $\lambda \tau_{ideal}$, the cooling circuit can be treated with the conventional formulation, and the ideal transit time and production rates can be safely adopted. On the contrary, with high values of $\lambda \tau_{ideal}$, the behaviour of the system deviates from conventional formulation, and a τ_{eff} lower than τ_{ideal} is obtained, while R_{eff} becomes lower than R_{ideal}. It is therefore clear how, in these cases, the adoption of CFD calculations to define proper transit time and production rates is required to ensure the accuracy of the results, due to the interaction between radionuclide production and decay and fluid-dynamic aspects.

5.2. Transport analysis results

The transport analyses of the considered nuclides inside the PFCs and CB PHTSs were assessed by running transient 1D analyses, by adopting the methodology described in section 2.

The nodalization adopted for the PFCs PHTS foresees 48 in-flux nodes, treated by implementing equation (7) in the MATLAB-Simulink environment, and 229 nodes not under neutron flux, namely several sections of the hot and cold rigs, the feeders, several sections of the hot and cold legs, and the HXs. These components are treated with the same 1D, conventional approach, by adopting equation (5) without the source term and considering the ideal transit time. Regarding the CB PHTS, its nodalisation is made of 48 in-flux nodes and 238 ex-flux nodes, treated as for the PFCs PHTS. Moreover, concerning the timestep adopted for the analyses, values lower than the smallest transit time among the different nodes have been considered. A sketch of the MATLAB-Simulink model of the PFCs PHTS is shown in figure 16.

Equations (7) and (5) are solved for all the nodes in figure except for the green ones, where it is simply calculated the mixing of concentrations weighted on mass flow rates coming from parallel branches.

The concentrations of ^{16}N, ^{17}N, and ^{19}O inside the divertor PHTSs reach quickly saturation conditions, in a period of time significantly shorter than the plasma pulse. The reason is that the time constants involved in the studied phenomenology are rather different from each other, more precisely the duration of the source pulse is much larger than the transit time T of the water in the investigated PHTSs, that can be estimated around 22 and ≈ 70 s respectively for the PFCs and the CB systems, and these time periods are larger than (for ^{16}N and ^{17}N) or comparable to (^{19}O) the lifetimes of the considered short-lived radionuclides. Figures 17 and 18 show the saturation concentrations of these isotopes respectively in the PFCs and CB PHTSs.

As far as ^{41}Ar is concerned, the transient is relatively longer and equal to about ~5 periods of the pulsed source as shown in figure 19, where the time profile of the ^{41}Ar concentration for the PFCs PHTS outside the bioshield is reported as an example. In the figure, it is easy to recognize in the small peaks that follow each other the effect of the dwell phase of the source.
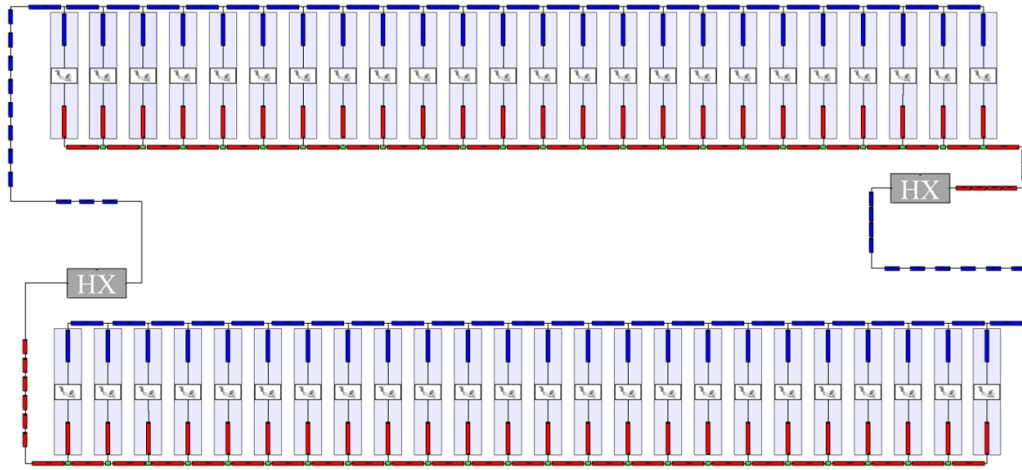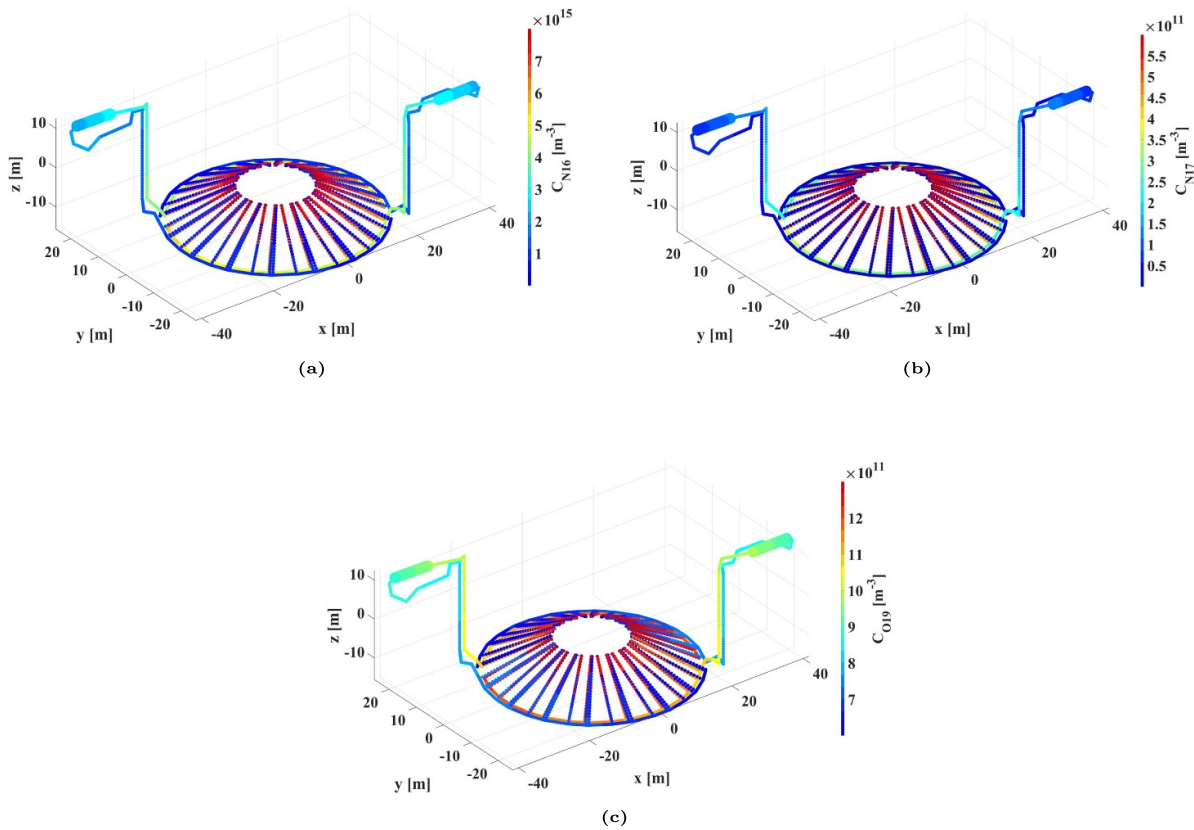
Figure 16. MATLAB-Simulink model of the PFCs PHTS.

Figure 17. ^{16}N (*a*), ^{17}N (*b*), and ^{19}O (*c*) concentrations in the PFCs PHTS.

The saturation concentrations of ^{41}Ar in the PFCs and CB PHTSs are $1.69 \cdot 10^{11}$ m^{-3} and $4.26 \cdot 10^{12}$ m^{-3} respectively. These values are essentially uniform in the two loops as can be deduced by observing that the product of the decay constant of ^{41}Ar times the overall transit time of the two PHTSs is very small ($e^{-\lambda T} \approx 1$), so that concentration variations are negligible in the ex-vessel nodes and very small in the nodes under neutron flux.

Of course, ^{14}C, given its enormous half-life, cannot saturate and it is not possible to employ the MATLAB-Simulink model to evaluate these concentrations due to the huge amount of computational time that would be required. ^{14}C concentrations in the two circuits after 6 Full Power Years (FPYs), that is the expected life of the reactor, can be assessed by simple algebraic formula, obtained by linearizing equation (5), and are respectively $3.62 \cdot 10^{20}$ m^{-3} and $1.00 \cdot 10^{22}$ m^{-3} for the PFCs and CB PHTSs, essentially uniform in the two loops.

A summary of the maximum concentrations of the studied radioisotopes together with their volumetric activities A outside the bioshield is reported in table 7.
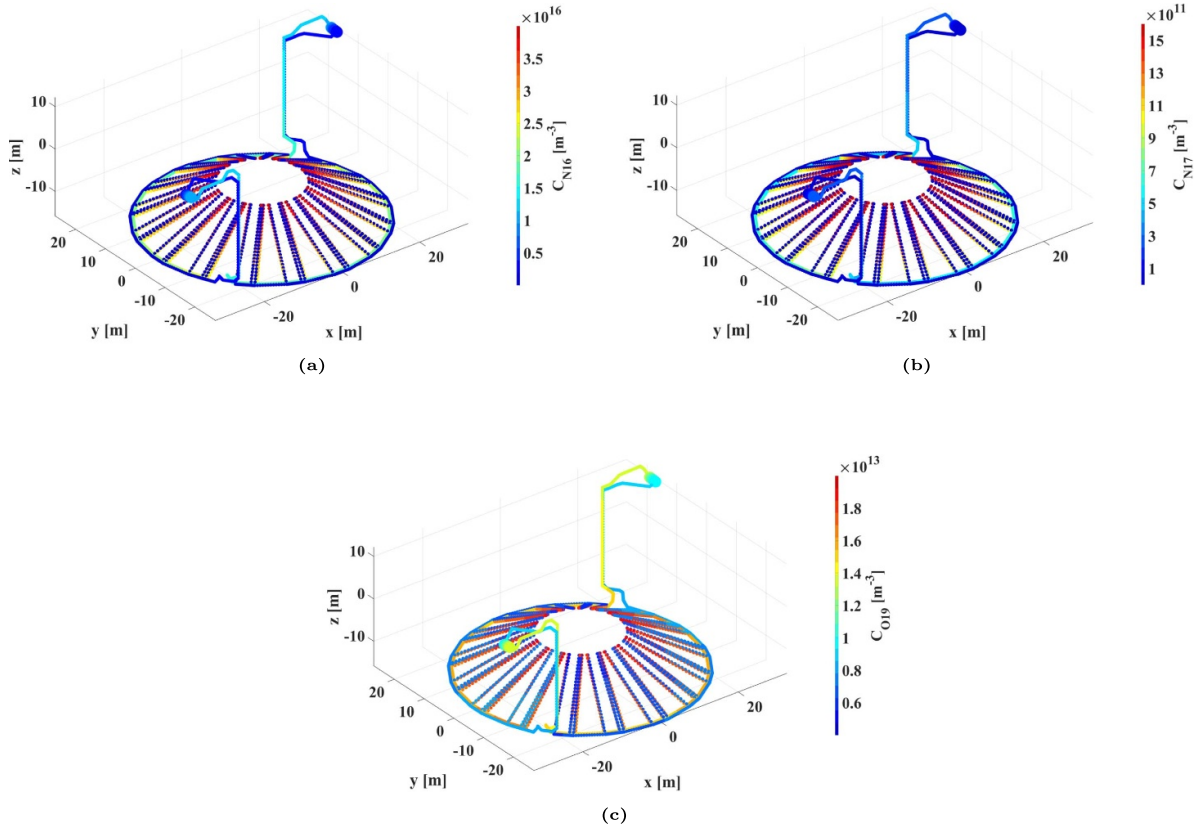
Figure 18. ^{16}N (*a*), ^{17}N (*b*), and ^{19}O (*c*) concentrations in the CB PHTS.
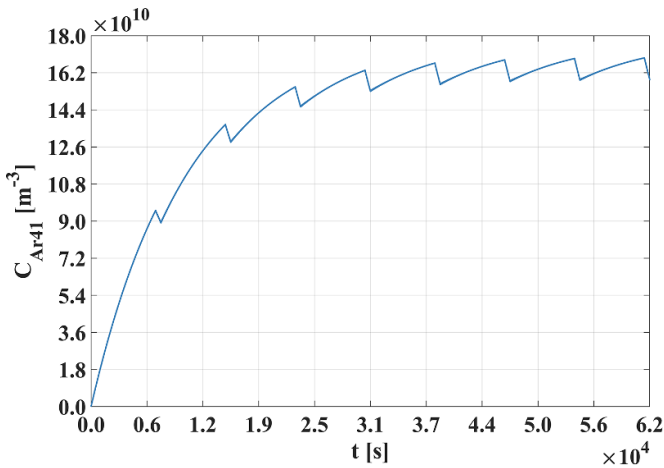

Figure 19. ^{41}Ar concentration time profile outside the bioshield for the PFCs PHTS.

5.3. Discussion

As already pointed out in section 5.1, the interaction between the radionuclide productionroving the estimation of activatio and decay and fluid-dynamic phenomena becomes relevant when the product $\lambda\tau_{\text{ideal}}$ is high. To assess the error that would be introduced by not relying on the CFD characterization, a comparison between the concentration values obtained in section 5.2 and those obtained by adopting a conventional treatment of the in-flux components is performed. In particular, for the transport simulations with the conventional

Table 7. Maximum nuclide concentration and volumetric activity outside the bioshield.

		$C_{\max}$ (m^{-3})	$A_{\max}$ (Bq m^{-3})
^{16}N	PFCs	$3.02 \cdot 10^{15}$	$2.93 \cdot 10^{14}$
	CB	$1.25 \cdot 10^{16}$	$1.21 \cdot 10^{15}$
^{17}N	PFCs	$1.33 \cdot 10^{11}$	$2.21 \cdot 10^{10}$
	CB	$2.87 \cdot 10^{11}$	$4.77 \cdot 10^{10}$
^{19}O	PFCs	$9.80 \cdot 10^{11}$	$2.51 \cdot 10^{10}$
	CB	$1.37 \cdot 10^{13}$	$3.49 \cdot 10^{11}$
^{14}C	PFCs	$3.62 \cdot 10^{20}$	$1.39 \cdot 10^{9}$
	CB	$1.00 \cdot 10^{22}$	$3.85 \cdot 10^{10}$
^{41}Ar	PFCs	$1.69 \cdot 10^{11}$	$1.79 \cdot 10^{7}$
	CB	$4.26 \cdot 10^{12}$	$4.50 \cdot 10^{8}$

formulation, the in-flux nodes have been treated employing equation (5) with the transit time τ_{ideal} calculated with equation (6), while R_{ideal} values have been adopted as production rates.

The results obtained are reported briefly in table 8, showing a comparison in terms of maximum concentration outside the bioshield, together with the percentage difference ϵ between the results of the conventional model and those obtained with the CFD characterization.

As can be seen from the table, the relative difference between the two models is negligible in the case of the PFCs PHTS and for ^{41}Ar, while it can be observed that the conventional model significantly overestimates the

Table 8. Comparison between the results of the conventional model and the CFD characterization.

		$C_{\mathrm{max,conv}}$ (m^{-3})	$C_{\mathrm{max,CFD}}$ (m^{-3})	ε (%)
^{16}N	PFCs	$3.06 \cdot 10^{15}$	$3.02 \cdot 10^{15}$	1.5
	CB	$2.39 \cdot 10^{16}$	$1.25 \cdot 10^{16}$	91.7
^{17}N	PFCs	$1.36 \cdot 10^{11}$	$1.33 \cdot 10^{11}$	2.3
	CB	$6.10 \cdot 10^{11}$	$2.87 \cdot 10^{11}$	112.4
^{19}O	PFCs	$9.86 \cdot 10^{11}$	$9.80 \cdot 10^{11}$	0.6
	CB	$1.63 \cdot 10^{13}$	$1.37 \cdot 10^{13}$	19.1
^{41}Ar	PFCs	$1.69 \cdot 10^{11}$	$1.69 \cdot 10^{11}$	0.0
	CB	$4.26 \cdot 10^{12}$	$4.26 \cdot 10^{12}$	0.0

concentrations of ^{16}N, ^{17}N and ^{19}O inside the CB PHTS, up to a factor -2 for what concerns the two nitrogen species.

Although the usage of the conventional models seems to be conservative in terms of radioisotope concentration, it is clear that the adoption of CFD calculations is mandatory to obtain accurate results. Moreover, the magnitude of errors committed when using the conventional models is most likely dependent on the specific geometry of the problem, and it is therefore not possible to infer any general indication about these errors.

6. Engineering and safety considerations

The activation of the coolant and its impurities due to the passage through the reactor and exposition to high neutron fluxes is a topic which designers have dealt with since the early steps of nuclear energy use for heat and electric power applications [32]. When water is used as coolant, ^{16}N, ^{17}N and ^{19}O are the intrinsic activation products that present the highest activities in the loop. These short-lived products present no problem after reactor shutdown, but their high concentration prohibits access to the cooling system during plant operation and influences the shielding design for the equipment compartments and closest cubicles within the reactor building [33]. Furthermore, the radiation affects the lifetime of electrical insulation, lubricants, sealants, and elastomers used in the building. Radiation testing is necessary for the qualification of these materials [34].

Actually, ^{16}N is the isotope that substantially drives the shielding of the cooling loop equipment: wall thicknesses required to attenuate the high-energetic γs from ^{16}N are normally sufficient to stop γs and neutrons emitted by ^{19}O and ^{17}N, respectively, due to their lower penetrating power and source strengths. ^{17}N neutrons can activate the materials, introducing then an additional source of dose for operators during maintenance; in fission power plants, the residual activity induced via this channel in components and structures surrounding the cooling loop is generally negligible if weighted respect to the activity of corrosion products deposited onto the pipe walls of the circuit [35]; nonetheless analyses are on-going to quantify activation due to this neutron source.

Other radioisotopes from coolant activation such as ^{41}Ar and ^{14}C are not a concern during plant operation with regard to external radiation exposure and shielding purposes; in some cases, however, have to be taken into consideration being an important source term for plant discharges, dose assessment and radioactive waste management [35].

6.1. Shielding considerations related to intrinsic water activation

As discussed above, the coolant shield design will be mainly based on the activation of the oxygen isotopes contained in the water molecules. In fusion power plants, if compared to fission power plants, the much harder neutron spectrum exacerbates all the threshold reaction rates taking place within the coolant, leading to higher volumetric yields of production for isotopes like ^{16}N and ^{17}N.

Table 9 lists the specific activity of ^{16}N and ^{17}N isotopes at the exit of the active region for the DEMO divertor cooling loops as well as for relevant nuclear power plants (NPPs): a Westinghouse AP600 (W-AP600) PWR [36], a CANDU-6 [37], a combustion energy (CE) PWR [38], and the European pressurized reactor (EPR) [39].

From the analysis of table 9 it is not difficult to argue that shielding walls in fusion cooling systems will be thicker than in pressurized water reactors (PWRs) which need a shielding wall thickness of primary circuit components in the range 0.8–1.2 m [40].

6.2. Considerations on potential discharges of long-lived isotopes from water activation: the ^{14}C case

The design of any nuclear facility always ensures that releases of gaseous, liquid and solid wastes are minimized, although a small fraction of radionuclides do eventually escape the systems and are continuously discharged in various effluents. It is expected that in fusion power plants, notable airborne radioactive emissions will include mainly tritium and ^{14}C. However, some radioactive noble gases, volatile elements and particles might be present according to the specific features and working principles of the plant's auxiliary process systems.

At this early stage of DEMO design, any attempt to derive precise discharge limits for ^{14}C would probably end up in a speculative exercise not justified within the framework of this research activity, being the divertor cooling water only a part of the multiple ^{14}C sources in the DEMO plant. Nonetheless, a comparison of the production rates for this isotope in different nuclear plants can provide a useful starting point for future evaluations on the expected annual effluent discharges.

According to the production rates reported in table 3 for each DEMO divertor cassette, the production in the PFC coolant would be around 59 GBq per FPY, whereas in the CB water, a production rate as high as 1169 GBq/FPY might be reached.

As for comparison, the production in light water reactors (LWRs) coolant generally varies in the range 296–444 GBq/GWe/FPY [15], which implies that for an LWR with a thermal size comparable to DEMO [20] the annual production in coolant would be between 222 and 333 GBq. On the other hand, the yearly production of ^{14}C in CANDU reactors is notably higher due to the huge amount of moderator water under neutron flux and its higher enrichment in ^{17}O [41]. For

Table 9. ^{16}N and ^{17}N activities in DEMO Divertor and various NPPs at the exit of the active region.

Quantity	DEMO		W-AP600	CANDU-6	CE	EPR
	PFC	CB				
Nominal Power (MW)	2000 (fusion power)		1940	2061.4	2560	4500
Core/channel power density (W cm^{-3})	/	/	78.8	92.5	93	94.6
Neutron Wall Load (MW m^{-2})	1.03		/	/	/	/
In-flux zone transit τ (s)	1.30	44.33	1.00	0.79	0.78	0.85
Total loop transit T (s)	$\approx$22	$\approx$70	12.50	12.51	10.24	11.80
^{16}N activity (kBq g^{-1})	$8.40 \cdot 10^5$	$4.46 \cdot 10^6$	$6.03 \cdot 10^3$	$2.35 \cdot 10^3$	$7.41 \cdot 10^3$	$5.20 \cdot 10^3$
^{17}N activity (kBq g^{-1})	$1.17 \cdot 10^2$	$3.78 \cdot 10^2$	1.77	0.88	1.75	1.26

these reasons in a single CANDU-6 unit, the yearly production in heavy water is around 16 502 GBq, with only 222 GBq/FPY being produced in the primary heat transport system and the remaining 98.7% built up in the moderator circuit [42].

Both LWRs and heavy water reactors (HWRs) exhibit ^{14}C productions in their primary systems that are remarkably lower than the 1220 GBq/FPY produced in the DEMO divertor water. This is a direct consequence of the larger water inventory exposed to neutron irradiation in the DEMO divertor, which amounts to about 77 m^3; in a 2 GWth PWR, the water inventory in the core region is around 15 m^3, whereas a CANDU-6 contains approximatively 8 m^3 of heavy water under neutron flux in primary system coolant (heavy water under irradiation in moderator system ranges from 215 to 250 m^3) [43].

It seems evident that the decrease of water inventory under neutron flux would certainly help to minimize the production of this isotope that, in the current design configuration, would be generated at rates higher than the majority of NPPs.

7. Conclusions

This paper addresses the assessment of the spatial distribution of the water activation products along large hydraulic circuits of water-cooled nuclear reactors. Two large and complex hydraulic circuits such as the PHTSs of the DEMO divertor were examined. To this purpose an innovative method was developed that relies on neutronic calculations and a fluid-dynamic analysis based on a one-dimensional nodalization, in a MATLAB-Simulink environment, of the hydraulic circuit investigated, correlated with a CFD characterization on the nodes under neutron flux. More precisely, five activation products of the water constituents have been taken into

account: ^{16}N, ^{17}N, ^{19}O, ^{14}C, ^{41}Ar and their spatial distributions were assessed. The study showed that the results are influenced not only by the complexity of the geometries treated but also by the nature of the radioisotopes involved, as their mean lifetime affects their dynamic behaviour and thus the final results in terms of spatial distributions. This circumstance is due to the fact that the phenomenology investigated is characterised by three interacting time constants, the period of the source, the time required for the water to complete the given loop and, indeed, the mean lifetime of the radioisotopes. It is interesting to observe that a similar dynamic was found in a related work concerning the assessment of the polonium inventory in the liquid PbLi breeder loop of one of the blanket concepts envisaged for DEMO [19]. Finally, we conclude by noting that the results obtained highlight a couple of safety-related issues. One of them concerns the high concentration of ^{16}N, especially when compared to that of NPPs, which could pose serious constraints on the design of shielding in certain key positions of the reactor primary circuit. The other issue relates to the massive production of ^{14}C that should be addressed by appropriate design choices, maybe aimed at the minimization of water inventory under neutron flux.

Disclaimer

ORCID iDs

P. Chiovaro ⬤ https://orcid.org/0000-0002-2851-9600
A. Quartararo ⬤ https://orcid.org/0000-0002-1006-6084
S. Giambrone ⬤ https://orcid.org/0000-0003-0173-3460
E. Vallone ⬤ https://orcid.org/0000-0002-2309-6119

References

[1] 2012 *Modelling of Transport of Radioactive Substances in the Primary Circuit of Water Cooled Reactors (TECDOC Series)* (INTERNATIONAL ATOMIC ENERGY AGENCY) p 1672

[2] Chiovaro P. *et al* 2020 Investigation of the DEMO WCLL breeding blanket cooling water activation *Fusion Eng. Des.* **157** 111697

[3] Berry T.A., Nobs C.R., Dubas A., Worrall R., Eade T., Naish J. and Packer L.W. 2021 Integration of fluid dynamics into activation calculations for fusion *Fusion Eng. Des.* **173** 112894

[4] Moreno Carrero C., Cau F. and Pampin R. 2022 Radio-species transport model for coupled fluid dynamics-neutron activation calculations *Fusion Eng. Des.* **181** 113171

[5] De Pietri M., Alguacil J., Rodríguez E. and Juárez R. 2023 Development and validation in water of FLUNED, an open-source tool for fluid activation calculations *Comput. Phys. Commun.* **291** 108807

[6] Caruso G. *et al* 2022 DEMO The main achievements of the Pre—Concept phase of the safety and environmental work package and the development of the GSSR *Fusion Eng. Des.* **176** 113025

[7] Terranova N. and Di Pace L. 2021 DEMO WCLL primary heat transfer system loops activated corrosion products assessment *Fusion Eng. Des.* **170** 112456

[8] X-5 Monte Carlo Team 2003 *MCNP—A General Monte Carlo N-Particle Transport Code, Version 5* (LANL)

[9] Plompen A J *et al* 2020 The joint evaluated fission and fusion nuclear data library, JEFF-3.3 *Eur. Phys. J. A* **56** 181

[10] The MathWorks Inc. 2022 *Simulink Version: 10.6 (R2022b)* (available at: www.mathworks.com)

[11] ANSYS Inc. 2021 *ANSYS CFX-Solver Theory Guide* Release: 2021 R1 (Canonsburg, PA, USA: ANSYS, Inc.)

[12] Firestone R.B. 1999 *Table of Isotopes* 8th edn (Wiley)

[13] Jakhar S. 2016 Nuclear analysis of 16N and 17N radiation fields from TCWS activated water *ITER Neutronics Report* ITER IDM reference: ITER_D_QZ7BEK_v2.1 (Iter Organization)

[14] Taylor N., Ciattaglia S., Cortes P., Iseli M., Rosanvallon S. and Topilski L. 2012 ITER safety and licensing update *Fusion Eng. Des.* **87** 476–81

[15] Kim K., Palino G.F. and Helmolz H.R. 2010 Estimation of carbon-14 in nuclear power plant gaseous effluents *EPRI Report Id* 1021106 (Electric Power Research Institute)

[16] Salam M. and Elisabeth S. 2020 A study on radiation dose estimation of argon-41 and nitrogen-16 airborne released from the Kartini research reactor *J. Phys.: Conf. Ser.* **1436** 012046

[17] Federici G., Holden J., Baylard C. and Beaumont A. 2021 The EU DEMO staged design approach in the Pre-Concept Design Phase *Fusion Eng. Des.* **173** 112959

[18] You J.H. *et al* 2022 Divertor of the European DEMO: engineering and technologies for power exhaust *Fusion Eng. Des.* **175** 113010

[19] Chiovaro P. *et al* 2022 Production and transport modelling of Po-210 in DEMO reactor *Nucl. Fusion* **62** 056022

[20] Barucca L. *et al* 2021 Pre-conceptual design of EU DEMO balance of plant systems: objectives and challenges *Fusion Eng. Des.* **169** 112504

[21] Pampin R., Cau F., Fabbri M., Izquierdo J. and Portone A. 2021 Improving the estimation of activation levels in flowing liquids under irradiation and decay *Nucl. Fusion* **61** 036003

[22] Jeong N., Seo K., Chi D.-Y. and Yoon J. 2013 Estimation of flow residence time in a decay tank for a pool type research reactor using CFD *Nucl. Eng. Des.* **255** 162–8

[23] Bonavolontà U. *et al* 2020 EU-DEMO divertor: cassette design and PFCs integration at pre-conceptual stage *Fusion Eng. Des.* **159** 111784

[24] Di Maio P.A. *et al* 2021 Thermal-hydraulic study of the DEMO divertor cassette body cooling circuit equipped with a liner and two reflector plates *Fusion Eng. Des.* **167** 112227

[25] Di Maio P.A., Burlon R., Mazzone G., Quartararo A., Vallone E. and You J.H. 2021 Hydraulic assessment of an upgraded pipework arrangement for the DEMO divertor plasma facing components cooling circuit *Fusion Eng. Des.* **168** 112368

[26] Moscato I. 2022 *Divertor Cassette Body PHTS: Layout and Summary Tables* EUROfusion IDM Ref: 2Q2REP v1.0

[27] Moscato I. 2022 Divertor PFC PHTS: Layout and Summary Tables EUROfusion IDM Ref: 2Q3PQG v1.0

[28] Noce S. *et al* 2023 Neutronics assessment of the spatial distributions of the nuclear loads on the DEMO divertor ITER-like targets: comparison between the WCLL and HCPB Blanket *Appl. Sci.* **13** 1715

[29] Fischer U. and Qiu Y. 2020 *Material Compositions for PPPT Neutronics and Activation Analyses* EUROfusion IDM Ref.: 2MM3A6 v1.1

[30] Moro F. *et al* 2021 Nuclear performances of the water-cooled lithium lead DEMO reactor: neutronic analysis on a fully heterogeneous model *Fusion Eng. Des.* **168** 112514

[31] Moscato I. 2022 *Tokamak Thermal Power Flow* EUROfusion IDM Ref: 2Q3PUA v1.0

[32] Rockwell T. 1956 *Reactor Shielding Design Manual (TID)* (Van Nostrand)

[33] Solomon Y. 1978 *An Overview of Water Chemistry for Pressurized Water Nuclear Reactors* (T. Telford for BNES)

[34] Chiovaro P. *et al* 2020 Assessment of DEMO WCLL breeding blanket primary heat transfer system isolation valve absorbed doses due to activated water *Fusion Eng. Des.* **160** 111999

[35] Neeb K.H. 1997 *The Radiochemistry of Nuclear Power Plants With Light Water Reactors* (De Gruyter)

[36] Westinghouse Electric Company LLC 2000 *Radiation protection AP600-Design Control Document Tier 2* ch 12

[37] Societatea Nationala "Nucleareelectrica" SA 2005 *Final Safety Analysis Report for Cernavoda Unit-2* ch 12

[38] Florida Power & Light Company 1985 *Final Safety Analysis Report for St. Lucie-Unit 2* ch 11

[39] AREVA NP & EDF 2012 *Pre-Construction Safety Report for UK-EPR* ch 11

[40] Korea Electric Power Corporation, Korea Hydro & Nuclear Power Co., Ltd 2018 *Radiation protection APR1400-Design Control Document Tier 2* ch 12

[41] Sohn W., Kang D.W. and Chi J. 2004 Approaches for reducing carbon-14 stack emissions from Korean CANDU® nuclear power plant *J. Nucl. Sci. Technol.* **41** 235–46

[42] Atomic Energy Control Board, Advisory Committee on Radiological Protection 1995 *The management of carbon-14 in Canadian nuclear facilities*

[43] Sohn W., Kang D.-W. and Kim W.-S. 2003 An estimate of carbon-14 inventory at Wolsong nuclear power plant in the Republic of Korea *J. Nucl. Sci. Technol.* **40** 604–13